

## Prediction of local electric polarization using graph neural networks

Yuxing Ma ,<sup>\*</sup> Yingwei Chen ,<sup>\*</sup> Binhua Zhang, Yali Yang , Hongyu Yu , Xingao Gong, Yang Zhong ,<sup>†</sup> and Hongjun Xiang ,<sup>‡</sup>

*Department of Physics, Key Laboratory of Computational Physical Sciences (Ministry of Education), State Key Laboratory of Surface Physics, Institute of Computational Physical Sciences, Fudan University, Shanghai, 200433, China*



(Received 3 January 2025; revised 1 March 2025; accepted 7 March 2025; published 16 May 2025)

The calculation of electric polarization based on the Berry phase (BP) method plays a crucial role in understanding ferroelectric materials. However, it cannot capture local polarization within the supercell, especially in systems with complex topological structures such as flexoelectric structures and polar skyrmions. In this study, we present a method for calculating flexoelectric coefficients via graph neural networks (GNNs). We represent the polarization contribution of each unit cell to the overall supercell as the sum of the tensor contributions from each atom, while the tensor contribution from each atom can be represented as a linear combination of the local spatial components projected along the edge directions of a cluster centered on that atom. The local polarization can be obtained using GNNs without density-functional theory calculations. Using this method, we accurately calculate the flexoelectric coefficients in BaTiO<sub>3</sub> and Si, as well as the polarization distribution in the PbTiO<sub>3</sub>/SrTiO<sub>3</sub> superlattice. Our method provides a practical approach for local contributions of electric polarization calculations in large-scale systems.

DOI: [10.1103/PhysRevB.111.184105](https://doi.org/10.1103/PhysRevB.111.184105)

### I. INTRODUCTION

Polarization, as a fundamental property of materials, is a crucial concept for understanding the microscopic structure and physical behavior of materials. The flexoelectric effect is an important polarization phenomenon that has recently garnered significant attention in materials science. The flexoelectric effect [1–4] refers to the phenomenon where mechanical deformations, such as bending or stretching, lead to electrical polarization within the material. This effect is commonly observed in materials with low-symmetry crystal structures, such as certain ferroelectric materials [5,6], ceramics [7,8], and polymers [9–11]. The polarization induced by the strain gradient is not directly caused by the strain itself; this characteristic gives the flexoelectric effect a wide range of potential applications. For example, the flexoelectric effect can be applied in high-performance sensors and actuators [12,13], due to its high sensitivity to small deformations. Furthermore, this effect can be utilized to directly convert mechanical energy into electrical energy, contributing to the development of more efficient energy-harvesting systems [14,15]. It also offers a promising solution to overcome the limitations of traditional piezoelectric materials, such as the disappearance of piezoelectric properties at high temperatures or the reduction in piezoelectric response due to mechanical fatigue [16,17]. The flexoelectric coefficient is a parameter that quantifies the strength of the flexoelectric effect. Mathematically, the flexoelectric coefficient can be expressed as the relationship between the local polarization

( $\mathbf{P}$ ) within the material and the corresponding strain gradient ( $\nabla S$ ):  $\mathbf{P} = \mu \Delta S$ , from which the flexoelectric coefficient ( $\mu$ ) can be determined. Although the Berry phase (BP) method [18,19], based on the modern theory of polarization [20,21], can accurately predict the total polarization, it does not directly provide local polarization information to calculate the flexoelectric coefficient.

To calculate local polarization, an approximation method based on the Born effective charge (BEC) is often used. The BEC characterizes the polarization changes induced by ionic displacements [22,23], which enable the evaluation of local polarization through the product of BECs and atomic displacements. From the expansion of the electric polarization for the atomic displacements, the BEC is the first-order expansion of the polarization on the atomic displacements. Second-order or even higher-order terms may produce polarization contributions in some cases [24]. Moreover, the BECs of atoms in high-symmetric elementary systems are zero, so the local polarization of the distorted system cannot be evaluated. The high computational cost associated with the BP method and BEC calculations also limits their applicability to large complex systems, such as polar skyrmion [25–27] structures comprising numerous atoms. Therefore, alternative approaches are highly needed. Recent advancements in integrating machine-learning (ML) techniques with density-functional theory (DFT) have revolutionized the study paradigm in computational materials science [28–33]. Therefore, ML-based methods are expected to address this challenge in quantifying local polarization using the BP method and achieve DFT-level accuracy in large-scale systems.

In this study, we utilized graph neural networks (GNNs) to compute local polarization tensors based on the local geometric features of atoms. The total polarization, derived from the

<sup>\*</sup>These authors contributed equally to this work.

<sup>†</sup>Contact author: [yzhong@fudan.edu.cn](mailto:yzhong@fudan.edu.cn)

<sup>‡</sup>Contact author: [hxiang@fudan.edu.cn](mailto:hxiang@fudan.edu.cn)

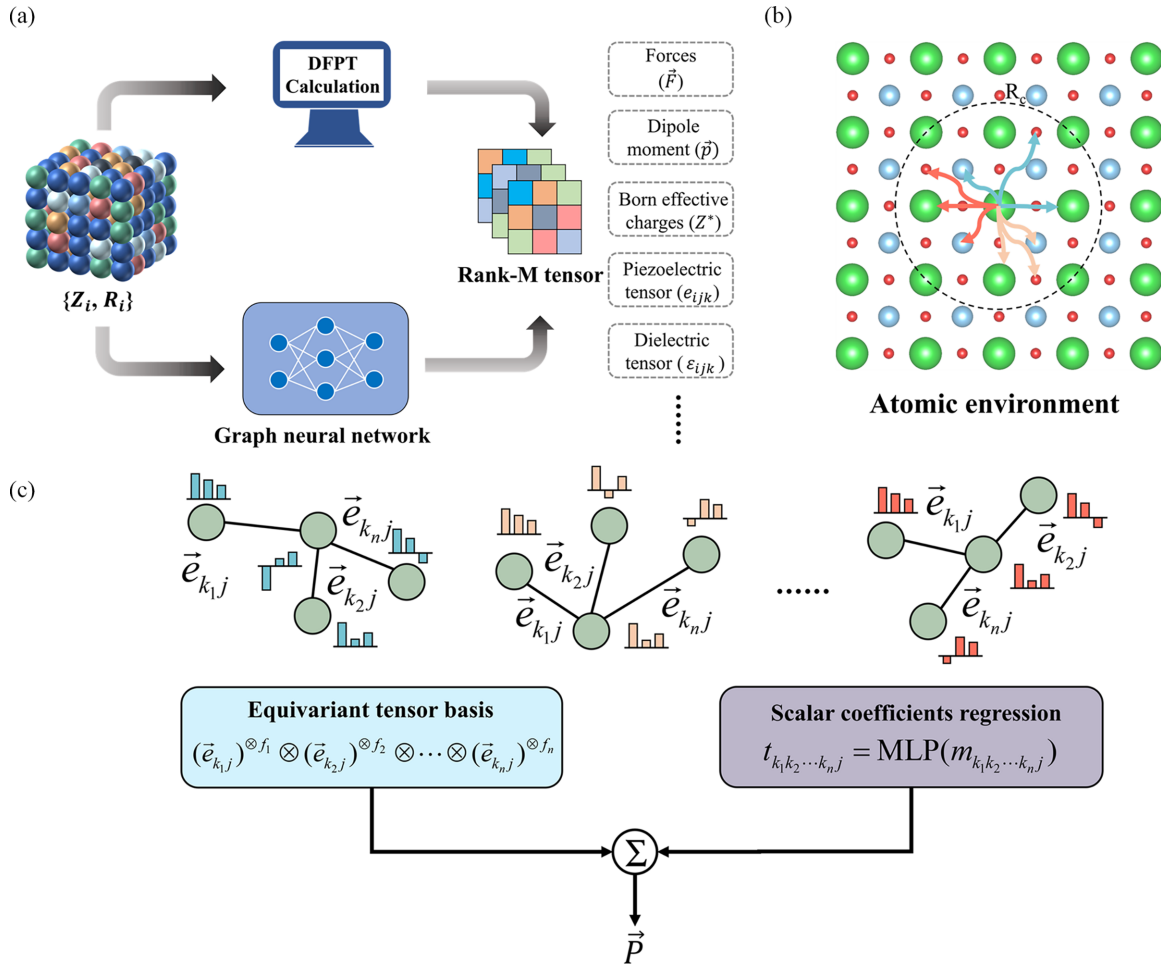


FIG. 1. An overview of the graph neural network for predicting the dipole moment tensor. (a) The graph neural network enables a direct mapping from the atomic structure  $\{R_i\}$  and elemental information  $\{Z_i\}$  to tensor properties of materials, thereby bypassing the computationally intensive DFPT calculations. (b) Each atomic tensor is influenced by the neighboring atoms within  $R_c$ . In the case of the Born effective charge tensor, local charge neutrality in the atomic environment requires that the BEC of the target ion be balanced by the charges of the surrounding ions. (c) The scalars  $t_{k_i j}$  and the unit edge vectors  $\vec{e}_{k_i j}$  from the neighboring atom  $k_i (i \in N)$  to the central atom  $j$  are aggregated into the cluster features. The atomic rank- $M$  tensors are expanded with the rank- $M$  tensor bases constructed by  $M$  edge vectors. The equivariant tensor bases are built by unit edge vectors  $\vec{e}_{k_i j}$  through tensor-basis construct block, and  $(\vec{e}_{k_i j})^{\otimes f_i}$  is the  $f_i$ -fold tensor product of  $\vec{e}_{k_i j}$  ( $\sum_{i=1}^n f_i = M$ ). The corresponding scalar coefficients  $t_{k_1 k_2 \dots k_n j}$  are obtained from cluster feature ( $m_{k_1 k_2 \dots k_n j}$ ) of the  $j$ -centered cluster through the regression block. The tensor of atom  $j$  is obtained by summing the tensor contributions of each neighbor.

summation of these predicted local polarization tensors, exhibits excellent agreement with the total polarization obtained from DFT calculations. Furthermore, we developed a method to determine the flexoelectric coefficient by evaluating the ratio of local polarization contributions to the strain gradient. Using our trained model, we have computed the flexoelectric coefficients for both BaTiO<sub>3</sub> and Si systems. By the same network weights, we accurately predicted dipole moment tensors across different cell sizes and crystal phases, thereby validating the transferability of our proposed method. Furthermore, we calculated the polarization distribution within the PbTiO<sub>3</sub>-SrTiO<sub>3</sub> superlattice and observed the formation of polar skyrmion bubbles and ferroelectric domain walls. This research offers an efficient approach to accelerate the computation of local electric polarization in large-scale systems while preserving *ab initio* accuracy.

## II. METHODS

We have developed an equivariant GNN model that can realize direct mapping from atomic structure  $\{R_i\}$  and elemental information  $\{Z_i\}$  to the tensors properties of the material without time-consuming *ab initio* computations, as shown in Fig. 1(a). The central idea of this network is to represent the rank- $M$  tensor property of a crystal as the average of the atomic rank- $M$  tensor contributions, as expressed by Eq. (1):

$$T^M = \sum_{j=1}^N T_j^M, \quad (1)$$

where  $N$  is the number of atoms in the cell. The atomic tensor can be represented by projecting it onto the local spatial components along the edge directions of multiple-sized clusters

and then linearly combining these components, as shown in Eq. (2):

$$T_j^M = \sum_{k_i \in N(j)} t_{k_1 k_2 \dots k_n j} (\vec{e}_{k_1 j})^{\otimes f_1} \otimes (\vec{e}_{k_2 j})^{\otimes f_2} \otimes \dots \otimes (\vec{e}_{k_n j})^{\otimes f_n}, \quad (2)$$

where  $N(j)$  represents the set of all neighbor atoms within cutoff  $R_c$ ,  $\vec{e}_{k_n j}$  represents the unit edge vector from the neighbor atom  $k_n$  to atom  $j$ ,  $(\vec{e}_{k_n j})^{\otimes f_n}$  represents the  $f_n$ -fold tensor product of  $\vec{e}_{k_n j}$  ( $\sum_{i=1}^n f_i = M$ ), and  $t_{k_1 k_2 \dots k_n j}$  is the corresponding scalar coefficient. The dipole moment, being a first-order tensor (i.e., a vector), can be expressed based on Eq. (1) and Eq. (2) as follows:

$$\vec{p}_j = \sum_{k \in N(j)} c_{kj} \vec{e}_{kj}, \quad (3)$$

where the coefficient  $c_{kj}$  represents the magnitude of the dipole moment for each atom.

In our approach, the total electric polarization is expressed as the sum of atomic contributions; however, the polarization contribution of individual atoms cannot be quantified explicitly. This is similar to the case of interatomic potential, where the total energy of the system is calculated as the sum of the energies of all atoms, even though the energy of a single atom does not have a well-defined physical meaning. For a unit cell (u.c.), the total polarization is obtained by summing the polarization contributions of individual atoms, and it can be fitted by our network using the polarization values derived from BP calculations. For a supercell (sc), the total polarization scales linearly with the system size, i.e.,  $P^{sc} = \sum_i P_i^{u.c.}$ , and the translational symmetry of the GNN ensures that the polarization per unit cell remains consistent with DFT calculations.

The detailed architecture of the GNN is shown in Fig. S1 [34]; the GNN first embeds the atom types  $Z_i$ , interatomic distances  $\|\vec{r}_{ij}\|$ , and relative orientations  $\vec{r}_{ij}$  into the initial feature vectors  $V_i^0$  and  $V_j^0$ , where the interatomic distances are expanded using Bessel basis functions. The GNN uses a directional message-passing framework like DIMENET++ [35] and introduces an additional triplet component into the crystal graph to construct cluster features. When constructing initial tensor features, we follow the “atomic locality” principle, whereby the atomic tensor is determined only by the atomic environment, independent of the entire system, as shown in Fig. 1(b). For instance, the BEC tensor of an ion is influenced by its neighboring atoms due to the intrinsic requirement of local charge neutrality. Based on the above derivation of tensor property prediction, we construct two network blocks for constructing equivariant tensor basis and scalar coefficients predictions, as shown in Fig. 1(c). Multiple edge vectors are utilized to construct the tensor basis through the equivariant tensor-basis block, which consists of multiple equivariant convolution layers. The corresponding scalar coefficients are mapped from the features of each cluster using a scalar coefficient regression block, which is composed of multiple multilayer perceptrons. With the iteration of multiple convolution layers, more and more atomic information will be aggregated into the features, thereby realizing the update of node and edge features. Since physical properties

inherently satisfy equivariance, our equivariant network naturally fulfills this requirement. By incorporating equivariance into our network architecture, we ensure that any changes or transformations observed in the physical properties are accurately captured and represented by our model. In the following section, we will demonstrate the accuracy and computational efficiency of the proposed framework in predicting local polarization tensors for BaTiO<sub>3</sub>, Si, and large-scale PbTiO<sub>3</sub>/SrTiO<sub>3</sub> superlattices.

### III. RESULTS

#### A. Flexoelectricity in BaTiO<sub>3</sub> and Si

To calculate the flexoelectric coefficient using our model, we train the GNN model in BaTiO<sub>3</sub> and diamond-silicon systems. We employ *ab initio* molecular dynamics (AIMD) simulations and structural perturbations to generate random configurations, which are subsequently utilized for constructing training sets through density-functional perturbation theory (DFPT) calculations. Here, we use the frame of ALLEGRO [36] as the machine-learning interatomic potential (MLIP) for the structural relaxation of large-scale structures.

BaTiO<sub>3</sub> has been extensively researched due to its remarkable ferroelectric properties, which makes it a promising material for various applications including electronics, energy-harvesting technology, telecommunications, and even biomedicine [37–39]. The GNN model was trained on a dataset of approximately 2200 different phase configurations of BaTiO<sub>3</sub>, including cubic (C), rhombohedral (Rh), and tetragonal (Te) phases. The dataset for MLIP training consisted of approximately 1100 samples. The two datasets were divided into the training set, test set, and validation set in a ratio of 0.8:0.1:0.1. The trained MLIP model achieved a mean absolute error (MAE) of 2.38 meV/Å for force and 0.245 meV per atom for energy in the test sets, with detailed results available in Table S3 [34]. As shown in Fig. 2(a), a comparison is presented between the dipole moment calculated based on the BP method and those predicted by our GNN model. Our predictions for the various dipole moment components show strong agreement with the DFT calculations, achieving the MAE of 0.025 e Å in the test sets. By outputting the value of each node in the GNN, the predicted dipole moment of the individual atom could be obtained. To illustrate this process, we randomly selected a structure from the AIMD trajectory for prediction and visualized it as a vector field, as depicted in Fig. 2(b). By summing the dipole moments of the atoms within each unit cell, we could calculate the dipole moment contribution of each unit cell to the overall polarization of the superlattice.

Flexoelectricity (FE) differs from the piezoelectric (PE) effect in that PE relates uniform strain to polarization, while FE relates strain gradients to polarization [40,41]. In the flexoelectric model, the polarization induced by flexoelectricity is introduced by applying a full-period trigonometric displacement to the atoms, followed by structural relaxation to eliminate the internal strain. This ensures that the polarization is caused by the strain gradient rather than the strain itself. By outputting the atomic dipole moment tensors through the GNN, the local dipole moment for each unit cell is obtained.

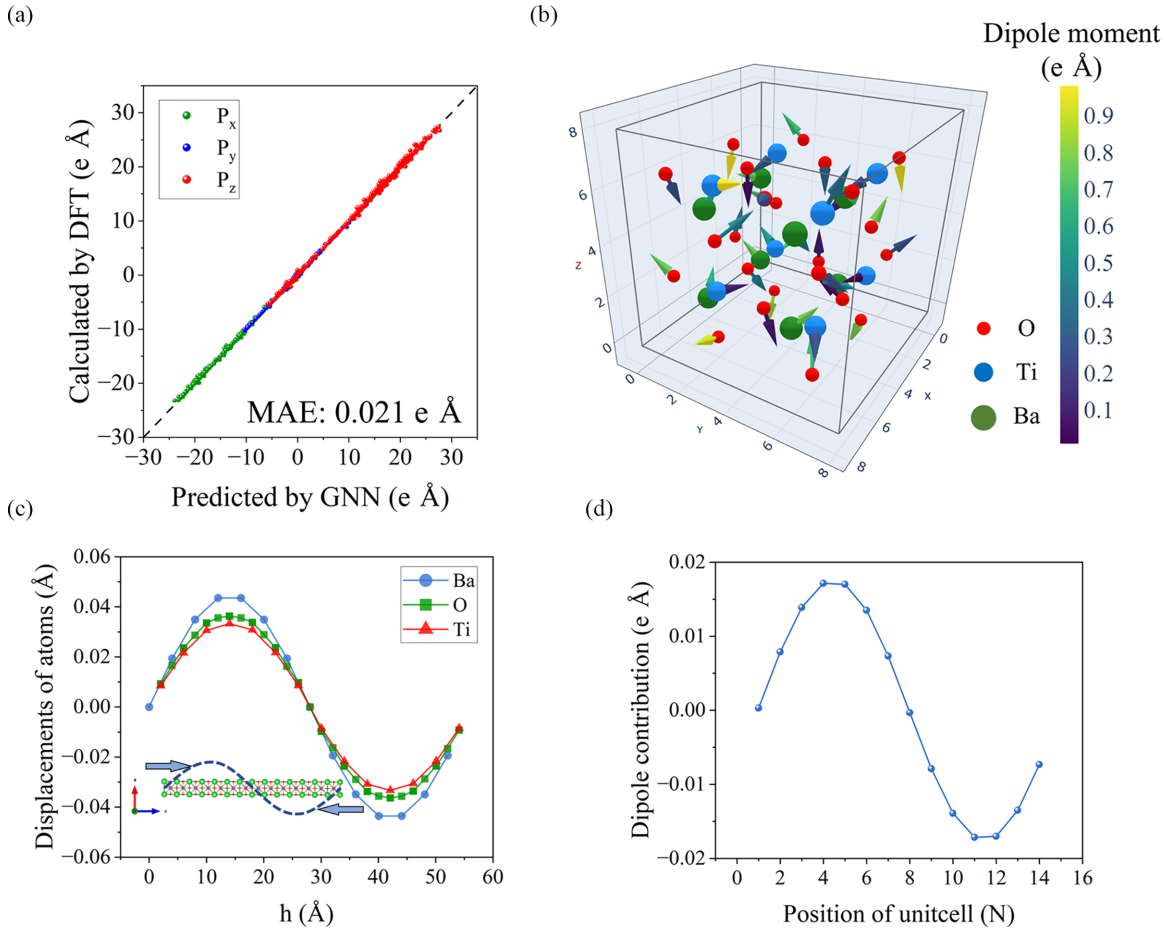


FIG. 2. (a) Comparison of the GNN model-predicted dipole moment with the DFT calculated on the test set for BaTiO<sub>3</sub>. (b) The well-trained GNN model predicts each atomic dipole moment for a random configuration from the molecular dynamics trajectory (the arrow direction represents the dipole orientation, while the color indicates the magnitude of the dipole moment corresponding to the color bar). The dipole moment for each unit cell is calculated by summing the dipole moments of all atoms within that cell. (c) The atomic displacements along the *c* axis for various species after structural relaxation. The arrows indicate the applied strain along the *c* axis for a 1 × 1 × 14 superlattice in the longitudinal flexoelectricity model of BaTiO<sub>3</sub> and the maximum strain is set to 0.5%. (d) The dipole moment of each unit cell in the longitudinal flexoelectricity model of BaTiO<sub>3</sub>.

Subsequently, the flexoelectric coefficient can be calculated by the ratio of local polarization to the strain gradient. The detailed flexoelectric coefficient calculation method is provided in the Supplemental Material [34]. To accurately calculate the flexoelectric coefficient, it is crucial to consider large cells [40]. We constructed a 1 × 1 × 14 flexoelectric supercell of BaTiO<sub>3</sub> and applied sinusoidal displacements to the atoms along the *c*-axis direction while fixing the position of the Ba atom. This induces periodic and uniform strain gradients in the superlattice structure. The displacement of various types of atoms within the supercell after structural relaxation is shown in Fig. 2(c). The polarization distribution along the *c* axis of each unit cell in the supercell is illustrated in Fig. 2(d). By choosing the unit cell in the  $\frac{h}{4}$  or  $\frac{3h}{4}$  position of the supercell along the *c*-axis direction ( $h$  is the length of the supercell in the *c*-axis direction), where the piezoelectric effect is absent and the strain gradient is maximum, the longitudinal flexoelectric coefficient ( $P$ ) was calculated by the following formula:

$$P_3 = \mu_{3333} \frac{\partial \varepsilon_{33}}{\partial x_3}, \quad (4)$$

where  $P_3$  represents the component of polarization of unit cell along the *c*-axis direction,  $\frac{\partial \varepsilon_{33}}{\partial x_3}$  represents the strain gradient induced by applying strain in the *c*-axis direction, and  $\mu_{3333}$  is the longitudinal flexoelectric coefficient. The calculated longitudinal flexoelectric coefficient is -0.758 nC/m, which is slightly larger than the values reported (~-0.36 nC/m) in previous studies [40,41]. The reason is that the local dipole moment calculated using BECs derived from the perfect unit cell of bulk BaTiO<sub>3</sub> is lower than the true polarization. In contrast, the dipole moment results obtained using our ML method are almost identical to those calculated using the BP method. For a more detailed discussion, please refer to Tables S4 and S5, and the associated analysis in Supplemental Material [34]. The additional flexoelectric coefficients for BaTiO<sub>3</sub>, calculated using the GNN model, are presented in Table S8. To assess the sensitivity of the GNN model, we constructed a 3 × 3 × 3 supercell and manipulated individual atoms of different elements by applying slight displacements, as shown in Fig. S2 [34] and by the results presented in Table S1. It can be observed that the GNN model captures the slight changes in dipole moments caused by small displacements

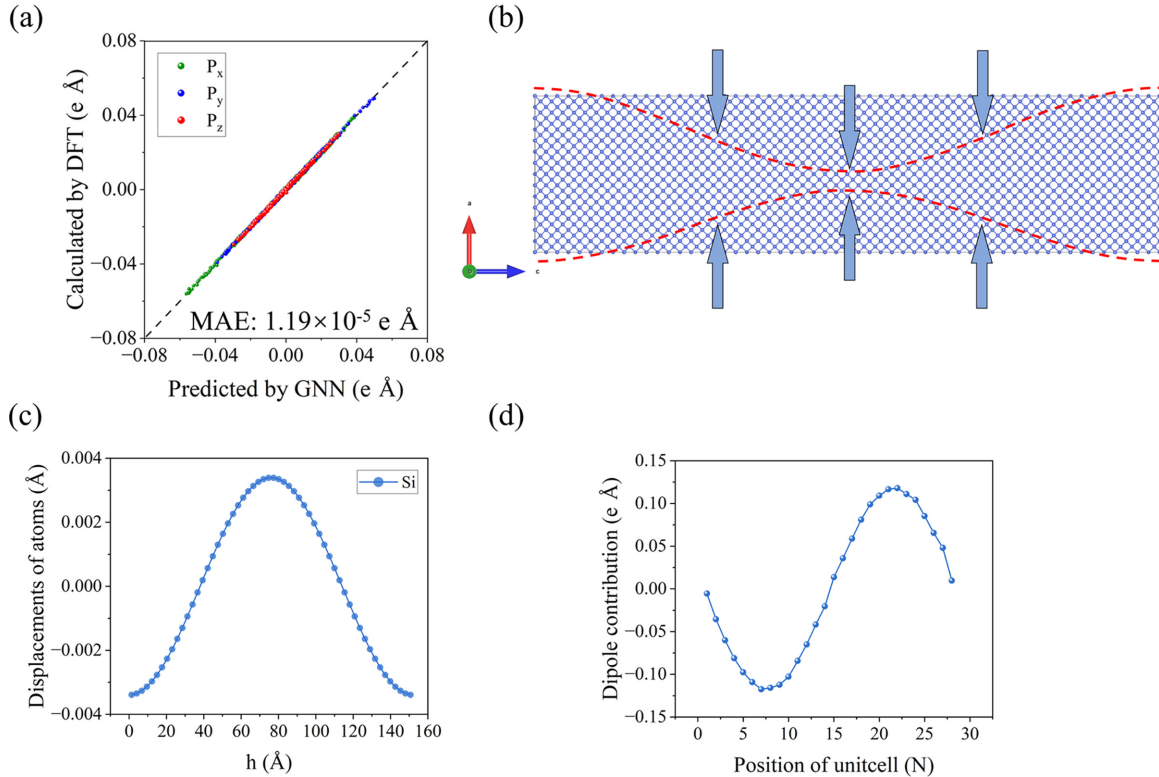


FIG. 3. (a) Comparison of the GNN model-predicted dipole moment with the DFT calculated on the test set for Si. (b) Structure of a  $7 \times 1 \times 28$  superlattice for the Si transverse flexoelectricity model. The arrows indicate the applied strain along the  $a$  axis and the maximum strain is set to 0.05%. (c) The displacement along the  $c$  axis for each silicon atom after structural relaxation. (d) The dipole moment distribution of each unit cell in the transverse flexoelectricity model of silicon.

of a single atom among many atoms. Furthermore, to test the generalization ability of the GNN model, we utilized the trained model to predict the dipole moment on the orthorhombic (O) structure of BaTiO<sub>3</sub>, which was not included in the training dataset. The test results are presented in Table S2 [34] and exhibit excellent generalization capability by using the same set of weight parameters to accurately predict BaTiO<sub>3</sub> structures across different crystal phases.

The BEC has limitations when dealing with the elementary system. Since the BECs are derivatives of polarization to atomic displacements, the charge distribution does not change with atomic displacements in the elementary system, resulting in zero BEC. Our GNN model, based on BP calculations, can solve this issue and compute the flexoelectric coefficient for Si. Silicon is widely used as the basic semiconductor material in traditional field-effect transistors due to its excellent electrical properties. However, silicon lacks piezoelectric properties, which means it cannot directly respond to mechanical signals. Nevertheless, the bending polarization induced by strain gradients in Si can effectively modulate the electronic transport properties of Si flexoelectric transistors [42]. We trained the GNN model for Si by using a dataset consisting of 1806 configurations from AIMD trajectories and perturbations. The MLIP model for Si, used for structural relaxation of large-scale structures, achieved the MAE of 5.03 meV/Å for force and 1.75 meV per atom for energy in the test sets, and detailed results can be found in Table S6 [34].

As shown in Fig. 3(a), the predicted dipole moment exhibits excellent agreement with those calculated by DFT. The trained GNN model achieves an MAE of  $1.19 \times 10^{-5}$  e Å for the dipole moment on the test set. We contracted a  $7 \times 1 \times 28$  transverse flexoelectric model and applied a cosine form strain along the  $a$ -axis direction, as shown in Fig. 3(b). The displacement of each Si atom within the supercell after structural relaxation is shown in Fig. 3(c). It indicates the presence of strain gradients, with the maximum strain occurring at the  $\frac{h}{2}$  position of the unit cell along the  $a$ -axis direction ( $h$  is the length of the supercell in the  $c$ -axis direction). The transverse strain will also generate a strain gradient in the  $c$ -axis direction, resulting in polarization  $P_3$  in this direction. The dipole moment of each unit cell along the  $c$  axis in the supercell is shown in Fig. 3(d). We were able to calculate the transverse flexoelectric coefficient of Si by the following formula:

$$\mu_{3311} = \frac{(P_{u.c.})_{\frac{3}{4}h} - (P_{u.c.})_{\frac{1}{4}h} + (P_3)_{\frac{1}{4}h} - (P_3)_{\frac{3}{4}h}}{\left(\frac{\partial \epsilon_{11}}{\partial x_3}\right)_{\frac{3}{4}h} - \left(\frac{\partial \epsilon_{11}}{\partial x_3}\right)_{\frac{1}{4}h}}, \quad (5)$$

where  $P_{u.c.}$  represents the polarization of the unit cell,  $P_3$  represents the component of  $P_{u.c.}$  along the  $c$ -axis direction, and  $\frac{\partial \epsilon_{11}}{\partial x_3}$  represents the strain gradient induced by applying stress in the  $a$ -axis direction;  $\mu_{3311}$  is the transverse flexoelectric coefficient. The transverse flexoelectric coefficient was calculated to be  $-0.566$  nC/m. The additional flexoelectric coefficients for silicon, obtained using our GNN, are pre-

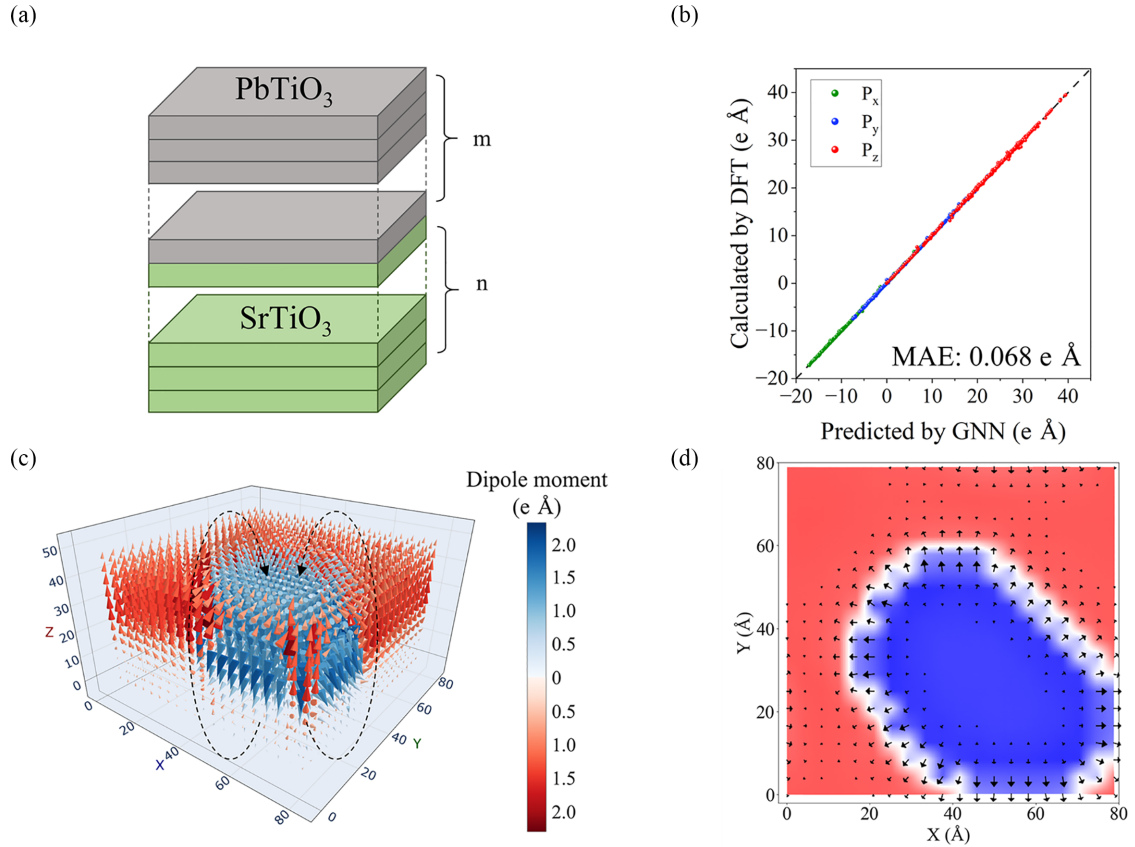


FIG. 4. (a) Schematic diagram of  $(\text{PbTiO}_3)_m/(\text{SrTiO}_3)_n$  superlattice. (b) Comparison of the predicted dipole moments from the GNN model with the DFT-calculated results for the test set of the  $\text{PbTiO}_3$ - $\text{SrTiO}_3$  superlattice system. (c) The polarization distribution of polar skyrmions in the  $(\text{PbTiO}_3)_8/(\text{SrTiO}_3)_4$  superlattice predicted by the trained GNN model. The color mapping in this panel indicates the  $z$  component of the dipole moment, with blue representing  $p_z < 0$  and red representing  $p_z > 0$ . (d) Cross-sectional view of the dipole moment projection in the  $x$ - $y$  plane, where blue and red regions, respectively, indicates the  $z$  component of the dipole oriented downward and upward.

sented in Table S9 [34]. Our model is capable of accurately calculating the flexoelectric properties in elementary systems.

### B. Polar skyrmions in $\text{PbTiO}_3/\text{SrTiO}_3$ superlattice

To demonstrate the capability of our model in handling very large systems, we selected the  $(\text{PbTiO}_3)_m/(\text{SrTiO}_3)_n$  superlattice system for testing. The discovery of room-temperature polar-skyrmion bubbles in lead titanate layers was made in  $(\text{PbTiO}_3)_m/(\text{SrTiO}_3)_n$  superlattice films [43–45]. The size of polar skyrmions typically ranges from a few nanometers, making them difficult to study through first-principles calculations. Usually, the displacement of Ti atoms is employed as an approximate estimate for the direction and magnitude of electric polarization within each unit cell in the supercell. We constructed structures of  $(\text{PbTiO}_3)_m/(\text{SrTiO}_3)_n$  superlattice, as shown in Fig. 4(a). The MLIP model of  $(\text{PbTiO}_3)_m/(\text{SrTiO}_3)_n$  superlattice was trained using 10 000 structures with different  $m:n$  stacking ratios to ensure its effectiveness in the structural relaxation of large systems. The error of forces and energies are shown in Table S7 [34]. The GNN model was trained using 1832 configurations, consisting of the structures of  $\text{PbTiO}_3$  (PTO),  $\text{SrTiO}_3$  (STO), and  $\text{PbTiO}_3$ - $\text{SrTiO}_3$ . The comparison of the dipole moment calculated by DFT and those predicted by GNN on the test set

is shown in Fig. 4(b); the GNN exhibits high accuracy of the superlattice and the MAE is  $0.068 \text{ e } \text{\AA}$ .

We constructed a superlattice structure of  $(\text{PbTiO}_3)_8/(\text{SrTiO}_3)_4$  and simulated its high-temperature annealing process using the trained MLIP model in LAMMPS software. The annealing process involved gradually cooling from 1000 to 1 K. Additionally, we utilized the GNN model to predict the dipole moment of each unit cell in an optimized low-temperature structure, which is visualized in Fig. 4(c). It can be observed that polar skyrmions have formed within the PTO layer, while the dipole moment of each unit cell in the STO layer is weaker compared to that in the PTO layer. From the cross-sectional view of dipole moment distribution within  $(\text{PbTiO}_3)_8/(\text{SrTiO}_3)_4$ , it can be observed that a hedgehog-like skyrmion has formed at the interface between STO and PTO and a Néel-like wall has emerged, as shown in Fig. 4(d) ( $x$ - $y$  plane) and Fig. S8 ( $x$ - $z$  plane) [34], consistent with the phenomenon reported previously [44,46]. The powerful capabilities exhibited by our model enable researchers to compute the dipole distribution of large crystal systems with *ab initio* level, which was previously challenging to access. Leveraging the flexibility and precision of our framework, our model can be extended to examine inhomogeneous domain-wall dielectric responses [47,48]. Additionally, it has the potential to investigate complex domain-wall textures

and topologically nontrivial polarization structures, including vortex states [49] and noncollinear dipole orders [50]. By combining our approach with nonequilibrium and other simulations, we can explore the behavior of domain walls and distinct textures in future research.

#### IV. CONCLUSIONS

We proposed a method for calculating the local polarization via GNNs bypassing the time-consuming DFT calculations. The GNN's capability to accurately capture the local polarization enabled us to further propose a method for calculating the flexoelectric coefficient. Our approach decomposed the total polarization tensor of a supercell into local tensor contributions from individual atoms, with atomic tensors represented as linear combinations of spatial components projected along cluster edges. We achieved highly accurate predictions of dipole moment tensors across different cell sizes and structural phases using the same network weights, and we computed the flexoelectric coefficient for BaTiO<sub>3</sub> and Si systems by using the trained model. We used our model to calculate the PbTiO<sub>3</sub>-SrTiO<sub>3</sub> superlattice; the appearances

of polar skyrmion pattern and ferroelectric domain walls are consistent with previous reports. This work offers a scalable and efficient solution for studying local polarization in large-scale ferroelectric systems.

#### ACKNOWLEDGMENTS

We acknowledge financial support from NSFC (Grant No. 12188101), the National Key R&D Program of China (Grant No. 2022YFA1402901), Shanghai Science and Technology Program (Grant No. 23JC1400900), the Guangdong Major Project of the Basic and Applied Basic Research (Future functional materials under extreme conditions—2021B0301030005), Shanghai Pilot Program for Basic Research—FuDan University 21TQ1400100 (Grant No. 23TQ017), and New Cornerstone Science Foundation.

The authors have no conflicts to disclose.

#### DATA AVAILABILITY

The data that support the findings of this article are openly available [59,60].

- 
- [1] T. D. Nguyen, S. Mao, Y.-W. Yeh, P. K. Purohit, and M. C. McAlpine, Nanoscale flexoelectricity, *Adv. Mater.* **25**, 946 (2013).
  - [2] P. Zubko, G. Catalan, and A. K. Tagantsev, Flexoelectric effect in solids, *Annu. Rev. Mater. Res.* **43**, 387 (2013).
  - [3] H. Wang, X. Jiang, Y. Wang, R. W. Stark, P. A. van Aken, J. Mannhart, and H. Boschker, Direct observation of huge flexoelectric polarization around crack tips, *Nano Lett.* **20**, 88 (2020).
  - [4] B. Wang, Y. Gu, S. Zhang, and L.-Q. Chen, Flexoelectricity in solids: Progress, challenges, and perspectives, *Prog. Mater Sci.* **106**, 100570 (2019).
  - [5] J. Narvaez, S. Saremi, J. Hong, M. Stengel, and G. Catalan, Large flexoelectric anisotropy in paraelectric barium titanate, *Phys. Rev. Lett.* **115**, 037601 (2015).
  - [6] P. Zubko, G. Catalan, A. Buckley, P. R. L. Welche, and J. F. Scott, Strain-gradient-induced polarization in SrTiO<sub>3</sub> single crystals, *Phys. Rev. Lett.* **99**, 167601 (2007).
  - [7] Y. Li, L. Shu, W. Huang, X. Jiang, and H. Wang, Giant flexoelectricity in Ba<sub>0.6</sub>Sr<sub>0.4</sub>TiO<sub>3</sub>/Ni<sub>0.8</sub>Zn<sub>0.2</sub>Fe<sub>2</sub>O<sub>4</sub> composite, *Appl. Phys. Lett.* **105**, 162906 (2014).
  - [8] L. Shu, M. Wan, Z. Wang, L. Wang, S. Lei, T. Wang, W. Huang, N. Zhou, and Y. Wang, Large flexoelectricity in Al<sub>2</sub>O<sub>3</sub>-doped Ba(Ti<sub>0.85</sub>Sn<sub>0.15</sub>)O<sub>3</sub> ceramics, *Appl. Phys. Lett.* **110**, 192903 (2017).
  - [9] S. Zhang, K. Liu, M. Xu, H. Shen, K. Chen, B. Feng, and S. Shen, Investigation of the 2312 flexoelectric coefficient component of polyvinylidene fluoride: Deduction, simulation, and mensuration, *Sci. Rep.* **7**, 3134 (2017).
  - [10] S. Zhang, X. Liang, M. Xu, B. Feng, and S. Shen, Shear flexoelectric response along 3121 direction in polyvinylidene fluoride, *Appl. Phys. Lett.* **107**, 142902 (2015).
  - [11] L. Shu, R. Liang, Z. Rao, L. Fei, S. Ke, and Y. Wang, Flexoelectric materials and their related applications: A focused review, *J. Adv. Ceram.* **8**, 153 (2019).
  - [12] X. Jiang, W. Huang, and S. Zhang, Flexoelectric nanogenerator: Materials, structures and devices, *Nano Energy* **2**, 1079 (2013).
  - [13] D. Akinwande *et al.*, A review on mechanics and mechanical properties of 2D materials—Graphene and beyond, *Extreme Mech. Lett.* **13**, 42 (2017).
  - [14] Z. Yan, Modeling of a piezoelectric/piezomagnetic nano energy harvester based on two dimensional theory, *Smart Mater. Struct.* **27**, 015016 (2018).
  - [15] X. Liang, S. Hu, and S. Shen, Nanoscale mechanical energy harvesting using piezoelectricity and flexoelectricity, *Smart Mater. Struct.* **26**, 035050 (2017).
  - [16] S. R. Kwon, W. B. Huang, S. J. Zhang, F. G. Yuan, and X. N. Jiang, Flexoelectric sensing using a multilayered barium strontium titanate structure, *Smart Mater. Struct.* **22**, 115017 (2013).
  - [17] K. L. Lee and A. K. Soh, Effects of electric fatigue on piezoelectric ceramics, *Key Eng. Mater.* **306–308**, 91 (2006).
  - [18] R. D. King-Smith and D. Vanderbilt, Theory of polarization of crystalline solids, *Phys. Rev. B* **47**, 1651 (1993).
  - [19] R. Resta, Macroscopic polarization in crystalline dielectrics: The geometric phase approach, *Rev. Mod. Phys.* **66**, 899 (1994).
  - [20] R. Resta and D. Vanderbilt, Theory of polarization: A modern approach, in *Physics of Ferroelectrics*, Vol. 105 (Springer, Berlin, 2007), pp. 31–68.
  - [21] R. Resta, Modern theory of polarization in ferroelectrics, *Ferroelectrics* **151**, 49 (1994).
  - [22] X. Gonze and C. Lee, Dynamical matrices, Born effective charges, dielectric permittivity tensors, and interatomic force constants from density-functional perturbation theory, *Phys. Rev. B* **55**, 10355 (1997).
  - [23] Ph. Ghosez, J.-P. Michenaud, and X. Gonze, Dynamical atomic charges: The case of ABO<sub>3</sub> compounds, *Phys. Rev. B* **58**, 6224 (1998).

- [24] J. B. Neaton, C. Ederer, U. V. Waghmare, N. A. Spaldin, and K. M. Rabe, First-principles study of spontaneous polarization in multiferroic  $\text{BiFeO}_3$ , *Phys. Rev. B* **71**, 014113 (2005).
- [25] S. Das *et al.*, Local negative permittivity and topological phase transition in polar skyrmions, *Nat. Mater.* **20**, 194 (2021).
- [26] R. Zhu *et al.*, Dynamics of polar skyrmion bubbles under electric fields, *Phys. Rev. Lett.* **129**, 107601 (2022).
- [27] T. Xu, Y. Ichiki, K. Masuda, Y. Wang, H. Hirakata, and T. Shimada, Ultrasmall polar skyrmions and merons in  $\text{SrTiO}_3$  heterostructures by polaron engineering, *ACS Nano* **17**, 10836 (2023).
- [28] S. Prateek, R. Garg, K. Kumar Saxena, V. K. Srivastav, H. Vasudev, and N. Kumar, Data-driven materials science: Application of ML for predicting band gap, *Adv. Mater. Process. Technol.* **10**, 708 (2024).
- [29] P. Reiser *et al.*, Graph neural networks for materials science and chemistry, *Commun. Mater.* **3**, 93 (2022).
- [30] K. Choudhary *et al.*, Recent advances and applications of deep learning methods in materials science, *npj Comput. Mater.* **8**, 59 (2022).
- [31] K. T. Butler, D. W. Davies, H. Cartwright, O. Isayev, and A. Walsh, Machine learning for molecular and materials science, *Nature (London)* **559**, 547 (2018).
- [32] Y. Zhong, S. Liu, B. Zhang, Z. Tao, Y. Sun, W. Chu, X.-G. Gong, J.-H. Yang, and H. Xiang, Accelerating the calculation of electron–phonon coupling strength with machine learning, *Nat. Comput. Sci.* **4**, 615 (2024).
- [33] Y. Zhong, H. Yu, J. Yang, X. Guo, H. Xiang, and X. Gong, Universal machine learning Kohn–Sham Hamiltonian for materials, *Chin. Phys. Lett.* **41**, 077103 (2024).
- [34] See Supplemental Material at <http://link.aps.org/supplemental/10.1103/PhysRevB.111.184105> for additional information, including details on the datasets, computational methods, machine-learning methods, flexoelectric coefficient calculations, accuracy tests of our GNN model, and additional results and discussions. The Supplemental Material also contains Refs. [36,40,41,51–58].
- [35] J. Gasteiger, S. Giri, J. T. Margraf, and S. Günnemann, Fast and uncertainty-aware directional message passing for non-equilibrium molecules, [arXiv:2011.14115v3](https://arxiv.org/abs/2011.14115v3) [cs.LG].
- [36] A. Musaelian, S. Batzner, A. Johansson, L. Sun, C. J. Owen, M. Kornbluth, and B. Kozinsky, Learning local equivariant representations for large-scale atomistic dynamics, *Nat. Commun.* **14**, 579 (2023).
- [37] Y. Jiang *et al.*, Enabling ultra-low-voltage switching in  $\text{BaTiO}_3$ , *Nat. Mater.* **21**, 779 (2022).
- [38] W. Qian, H. Wu, and Y. Yang, Ferroelectric  $\text{BaTiO}_3$  based multi-effects coupled materials and devices, *Adv. Electron. Mater.* **8**, 2200190 (2022).
- [39] X. Zhang, R. Xu, X. Gao, Y. Ji, F. Qian, J. Fan, H. Wang, W. Li, and H. Yang, Negative-pressure enhanced ferroelectricity and piezoelectricity in lead-free  $\text{BaTiO}_3$  ferroelectric nanocomposite films, *J. Mater. Chem. C* **8**, 8091 (2020).
- [40] J. Hong, G. Catalan, J. F. Scott, and E. Artacho, The flexoelectricity of barium and strontium titanates from first principles, *J. Phys.: Condens. Matter* **22**, 112201 (2010).
- [41] T. Xu, J. Wang, T. Shimada, and T. Kitamura, Direct approach for flexoelectricity from first-principles calculations: Cases for  $\text{SrTiO}_3$  and  $\text{BaTiO}_3$ , *J. Phys.: Condens. Matter* **25**, 415901 (2013).
- [42] D. Guo, P. Guo, L. Ren, Y. Yao, W. Wang, M. Jia, Y. Wang, L. Wang, Z. L. Wang, and J. Zhai, Silicon flexoelectronic transistors, *Sci. Adv.* **9**, eadd3310 (2023).
- [43] S. Das *et al.*, Pure chiral polar vortex phase in  $\text{PbTiO}_3/\text{SrTiO}_3$  superlattices with tunable circular dichroism, *Nano Lett.* **23**, 6602 (2023).
- [44] S. Das *et al.*, Observation of room-temperature polar skyrmions, *Nature (London)* **568**, 368 (2019).
- [45] A. Y. Abid *et al.*, Creating polar antivortex in  $\text{PbTiO}_3/\text{SrTiO}_3$  superlattice, *Nat. Commun.* **12**, 2054 (2021).
- [46] E. Zatterin *et al.*, Assessing the ubiquity of Bloch domain walls in ferroelectric lead titanate superlattices, *Phys. Rev. X* **14**, 041052 (2024).
- [47] S. Liu and R. E. Cohen, Origin of stationary domain wall enhanced ferroelectric susceptibility, *Phys. Rev. B* **95**, 094102 (2017).
- [48] A. Gurung, M. F. Ishtiyaq, S. P. Alpay, J. Mangeri, and S. Nakhmanson, Extrinsic dielectric response due to domain wall motion in ferroelectric  $\text{BaTiO}_3$ , *Comput. Mater. Today* **5**, 100016 (2025).
- [49] Q. Li *et al.*, Subterahertz collective dynamics of polar vortices, *Nature (London)* **592**, 376 (2021).
- [50] N. Wang, Z. Shen, W. Luo, H.-K. Li, Z.-J. Xu, C. Shi, H.-Y. Ye, S. Dong, and L.-P. Miao, Noncollinear ferroelectric and screw-type antiferroelectric phases in a metal-free hybrid molecular crystal, *Nat. Commun.* **15**, 10262 (2024).
- [51] G. Kresse and J. Furthmüller, Efficient iterative schemes for *ab initio* total-energy calculations using a plane-wave basis set, *Phys. Rev. B* **54**, 11169 (1996).
- [52] P. E. Blöchl, Projector augmented-wave method, *Phys. Rev. B* **50**, 17953 (1994).
- [53] G. Kresse and D. Joubert, From ultrasoft pseudopotentials to the projector augmented-wave method, *Phys. Rev. B* **59**, 1758 (1999).
- [54] J. P. Perdew, K. Burke, and M. Ernzerhof, Generalized gradient approximation made simple, *Phys. Rev. Lett.* **77**, 3865 (1996).
- [55] H. J. Monkhorst and J. D. Pack, Special points for Brillouin-zone integrations, *Phys. Rev. B* **13**, 5188 (1976).
- [56] A. Paszke *et al.*, PyTorch: An imperative style, high-performance deep learning library, [arXiv:1912.01703v1](https://arxiv.org/abs/1912.01703v1) [cs.LG].
- [57] A. Hjorth Larsen *et al.*, The atomic simulation environment—a Python library for working with atoms, *J. Phys.: Condens. Matter* **29**, 273002 (2017).
- [58] E. Bitzek, P. Koskinen, F. Gähler, M. Moseler, and P. Gumbsch, Structural relaxation made simple, *Phys. Rev. Lett.* **97**, 170201 (2006).
- [59] <https://zenodo.org/records/14587941>
- [60] <https://github.com/Yuxing0926/ETGNN>